APL Photonics

RESEARCH ARTICLE | SEPTEMBER 04 2024

Piezoelectrically driven Fano resonance in silicon photonics

Special Collection: Brillouin Scattering and Optomechanics

I. Ansari ; G. F. Feutmba ; J. P. George ; H. Rijckaert ; J. Beeckman ; D. Van Thourhout

APL Photonics 9, 096105 (2024)
https://doi.org/10.1063/5.0207482

Piezoelectrically driven Fano resonance in silicon photonics

Cite as: APL Photon. 9, 096105 (2024); doi: 10.1063/5.0207482
Submitted: 8 March 2024 • Accepted: 14 August 2024 •
Published Online: 4 September 2024

I. Ansari,[1,2,3] G. F. Feutmba,[1,2,3] J. P. George,[1,2,3] H. Rijckaert,[4] J. Beeckman,[2,3] and D. Van Thourhout[1,3,a)]

AFFILIATIONS

[1] Photonics Research Group, Department of Information Technology (INTEC), Ghent University-imec, 9052 Ghent, Belgium
[2] Liquid Crystal & Photonics Group, Department of Electronics and Information Systems (ELIS), Ghent University, 9052 Ghent, Belgium
[3] Centre for Nano and Bio-photonics, Ghent University, 9052 Ghent, Belgium
[4] Sol-gel Centre for Research on Inorganic Powders and Thin Films, Department of Chemistry, Ghent University, 9000 Ghent, Belgium

Note: This paper is part of the APL Photonics Special Topic on Brillouin Scattering and Optomechanics.
[a)] **Author to whom correspondence should be addressed:** dries.vanthourhout@ugent.be

ABSTRACT

Piezoelectric optomechanical platforms provide a promising avenue for efficient signal transduction between microwave and optical domains. Lead zirconate titanate (PZT) thin film stands out as a compelling choice for building such a platform given its high piezoelectricity and optical transparency, enabling strong electro-optomechanical transduction. This work explores the application of such transduction to induce Fano resonance in a silicon photonics integrated circuit (PIC). Our methodology involves integrating a PZT thin film onto a silicon PIC and subsequently removing the SiO_2 layer to suspend the silicon waveguide, allowing controlled mechanical vibrations. Fano resonances, characterized by their distinctive asymmetric line shape, were observed at frequencies up to 6.7 GHz with an extinction ratio of 21 dB. A high extinction ratio of 41 dB was achieved at the lower resonance frequency of 223 MHz. Our results demonstrate the potential of piezoelectric thin film integration for the generation of Fano resonances on passive photonic platforms such as Si, paving the way for highly sensitive, compact, and power-efficient devices relevant to a wide range of applications.

I. INTRODUCTION

A Fano resonance is observed in a system when a discrete resonance mode interferes with a continuous background, resulting in a sharp and asymmetric profile.[1] For a given quality factor of a resonator, a Fano resonance can lead to a sharper profile compared to the classical Lorentzian resonance from the standalone resonator. Owing to this distinctively sharp profile, a slight external perturbation in a Fano resonator can cause a significant amplitude and phase change in the Fano spectrum. This provides a powerful tool for ultrasensitive and power-efficient devices. In photonic integrated circuits (PICs), Fano resonances have been demonstrated primarily through waveguide-coupled microresonator systems,[2–7] photonic crystal cavities,[8–10] and plasmonic resonators[11,12] and are used in a wide range of applications such as sensing, low-power switching and modulation, slow-light devices, low-threshold lasing, and non-linear enhancement.[13,14] However, the fabrication of photonic crystal cavities remains challenging due to their reliance on strict fabrication tolerances. Plasmonic resonators have drawbacks such as optical loss and heat dissipation from their metallic components. While these Fano resonances were predominantly reported within the optical domain, the rapid growth of microwave photonics warrants the exploration of such mechanisms within the microwave domain.[15] For instance, Fano resonances can be exploited to create microwave-assisted reconfigurable photonic filters, modulators, and switches with very narrow passbands and steep roll-off characteristics.[16]

In this paper, we present a novel approach to generate a Fano resonance in a Si PIC using a piezoelectrically driven mechanism. We integrate a lead zirconate titanate (PZT) thin film on a Si PIC and undercut the device to harbor the mechanical vibration into the waveguide system. The unique synergy of strong electro-optic effect,[17] piezoelectric effect,[18] and optical transparency[19] within our

PZT film allows efficient electro-optomechanical interaction into the waveguide, rendering a Fano resonance in the microwave domain. Notably, the piezoelectric effect-based operation offers an additional degree of control through the electrical input. Hence, this work demonstrates a promising approach to achieve Fano resonances in passive photonics platforms (such as Si and SiN), which could lead to the development of highly sensitive and efficient devices that can be relevant in a wide range of applications, including sensing, filtering, modulation, switching, and microwave to optical conversion for quantum information processing.[13,20]

II. OPERATING PRINCIPLE

Integrated electro-optic modulators based on the Pockels effect are often implemented using a co-planar electrode design in which parallel electrodes are used to apply an electric field across the electro-optic material.[21] The optical mode is confined partially or completely inside a linear electro-optic material such as barium titanate ($BaTiO_3$), lead zirconate titanate ($PbZrTiO_3$), or lithium niobate ($LiNbO_3$). When an electric field is applied across the material, the effective index of the mode changes due to the electro-optic (EO) effect. Typically, these modulators show a broadband modulation response with their bandwidth limited by *RC*-effects (if the modulator length is substantially shorter than the RF wavelength), where *R* is the contact resistance and *C* is the capacitance of the device.

In this work, we demonstrate an electro-optomechanical transducer (EOMT), wherein the EO device is suspended by selectively etching the SiO_2 cladding layer, as illustrated in Fig. 1. The free suspension of the device enables a large mechanical perturbation in the structure, e.g., when driven through a piezoelectric transducer, resulting in a strong phase modulation. Contrary to the electro-optic (EO) effect, this phase modulation shows a strong frequency dependence, peaking at the mechanical resonance of the suspended structure. The mechanically induced phase modulation stems from different physical effects.

The suspended modulator harnesses a stronger strain-optic overlap in the waveguide without leaking mechanical energy into the substrate.[22] This gives a large optical phase modulation, particularly at the mechanical resonance, through the photoelastic effect (PE). In the suspended structure (large surface-to-volume ratio), a significant amount of the electric field from the optical mode is concentrated at the interfaces. This is due to a high permittivity contrast between the materials, such as Si and air. When the waveguide boundary is distorted, the field distribution changes. Hence, this so-called moving boundary (MB) effect also changes the effective mode index significantly at the mechanical resonance of the device. In addition, the radiation pressure from the input light distorts the suspended waveguide.[22,23] However, given that the laser power used for coupling light into our device is not very high (up to 14 dBm), this effect can be ignored. Therefore, the total index modulation for our suspended EOMT is given as follows:

$$\Delta n_{eff}^{tot} = \Delta n_{eff}^{EO} + \Delta n_{eff}^{PE} + \Delta n_{eff}^{MB}, \tag{1}$$

where Δn_{eff}^{EO}, Δn_{eff}^{PE}, and Δn_{eff}^{MB} are the effective index modulation from the EO, PE, and MB effects, respectively. At the mechanical resonance of the EOMT, the polarizability of the PZT (hence, n_{eff}^{EO}) changes slightly due to the electromechanical coupling. However, compared to Δn_{eff}^{PE} and Δn_{eff}^{MB}, which are strongly dependent on the mechanical deformation, Δn_{eff}^{EO} can be assumed to be frequency independent (see Appendix C). The frequency dependence of Δn_{eff}^{PE} and Δn_{eff}^{MB} can be expressed as follows:

$$\Delta n_{eff}^{PE} + \Delta n_{eff}^{MB} = \Delta n_0^{EM} \mathscr{L}(\Omega), \tag{2}$$

where Δn_0^{EM} is the amplitude of the index modulation associated with the electromechanical actuation, Ω is the applied RF (angular) frequency, and $\mathscr{L}(\Omega)$ is the frequency response. This index modulation [Eq. (2)] arises due to the piezoelectric driving of the EOMT, which can be regarded as a mechanical oscillator. Hence, this frequency response can be modeled as a driven oscillator response. Assuming that the linewidth (Γ) of the modulation response is much smaller than the resonance frequency (Ω_m), the frequency response near Ω_m can be approximated as Lorentzian,[20]

$$\mathscr{L}(\Omega) = \frac{\Gamma/2}{(\Omega - \Omega_m + j\Gamma/2)} = \frac{1}{\Delta\varepsilon + j}, \tag{3}$$

where $\Delta\varepsilon = \frac{(\Omega-\Omega_m)}{\Gamma/2}$ is the reduced frequency detuning.

From Eqs. (1)–(3),

$$\begin{aligned}\Delta n_{eff}^{tot} &= \Delta n_{eff}^{EO} + \frac{\Delta n_0^{EM}}{\Delta\varepsilon + j} \\ &= \Delta n_{eff}^{EO}\left(\frac{\Delta\varepsilon + \Delta n_0^{EM}/\Delta n_{eff}^{EO} + j}{\Delta\varepsilon + j}\right) \\ &= \Delta n_{eff}^{EO}\left(\frac{\Delta\varepsilon + q + j}{\Delta\varepsilon + j}\right),\end{aligned} \tag{4}$$

where $q = \Delta n_0^{EM}/\Delta n_{eff}^{EO}$ is the Fano or asymmetry parameter. The phase modulation amplitude for a modulator of length *L* is then

$$\begin{aligned}\alpha(L) &= \frac{2\pi L}{\lambda}|\Delta n_{eff}^{tot}| \\ &= D\left|\frac{\Delta\varepsilon + q + j}{\Delta\varepsilon + j}\right|, \\ \Rightarrow \alpha(L)^2 &= D^2\left(\frac{(\Delta\varepsilon + q)^2 + 1}{\Delta\varepsilon^2 + 1}\right),\end{aligned} \tag{5}$$

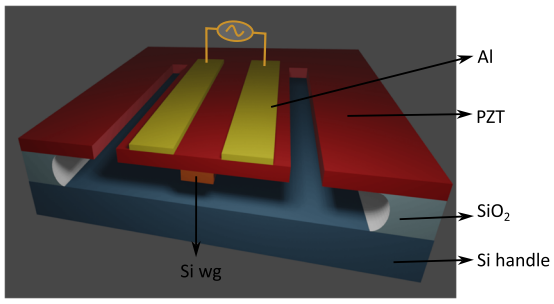

FIG. 1. 3D schematic of an electro-optomechanical transducer (EOMT).

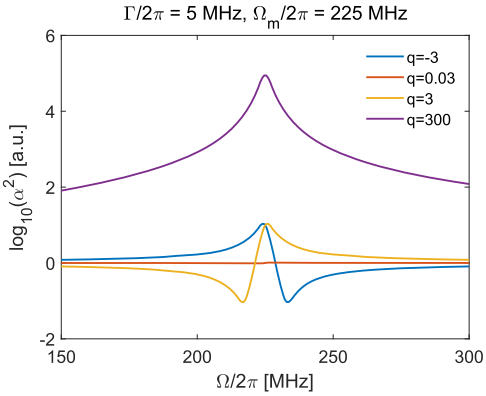

FIG. 2. Frequency response of the EOMT with different Fano parameters q.

where D = $\frac{2\pi L}{\lambda}\Delta n_{eff}^{EO}$ is a multiplication factor to the Fano expression. Figure 2 illustrates a log plot of Eq. (5) for different values of q. Here, the multiplication factor D was taken as unity for simplification. We can see that when $q \ll 1$, i.e., the broadband EO modulation is much stronger than the narrowband EM modulation, the frequency response is flat, as shown in a typical EO modulator. When $q \gg 1$, i.e., the EM modulation is much stronger than the EO modulation, the frequency response is Lorentzian, as shown in an acousto-optic modulator.[18,24] However, when the EO and EM modulation amplitudes are comparable, their interference produces a Fano shape in the frequency response. The polarity of the Fano curve relies on the sign of q.

III. FABRICATION OF THE SUSPENDED EOMT

The full process flow to fabricate the suspended devices is presented in Fig. 3. A silicon-on-insulator (SOI) chip with waveguide circuits was used as a starting sample. This chip was fabricated by imec in a multi-project wafer process,[25] where the waveguides were defined in a 220 nm thick silicon layer on top of a 2 μm buried SiO_2 layer, using deep UV (193 nm) lithography. The wafer was planarized using SiO_2 deposition and chemical mechanical polishing (CMP). Next, the wafers were diced into centimeter-scale samples.

The processing of the sample starts with ~ 400 nm PZT thin film deposition using the chemical solution deposition method as described in Ref. 26. This thickness was chosen based on our previous success in fabricating and demonstrating piezoelectric microelectromechanical system (MEMS) actuation with a similar PZT film.[27] Due to the high permittivity of the PZT, it was difficult to image the high-resolution alignment markers on the chip within the e-beam lithography tool. Therefore, the PZT film was partially etched in several regions that had e-beam markers defined in the silicon layer underneath. An optimized PZT reactive ion etching (RIE) recipe involving CHF_3, SF_6, Ar, and O_2 as reactant gases was used. Next, the electrodes were defined using e-beam lithography (to maintain high alignment accuracy), followed by Al deposition and a lift-off process. The contact pads were then patterned with optical lithography, followed by Al deposition and a lift-off process. In the next step, a 50 nm Al_2O_3 thin film was deposited on the sample using atomic layer deposition (ALD). This thin film was employed as a protection layer against the HF vapor used in the next step. In this sample, a layer of Ti35 was spin-coated, and the underetch windows were defined using UV lithography. After hard-baking the sample, first the Al_2O_3 thin film was etched with a diluted 1% (by volume) buffered hydrogen fluoride (BHF) solution, followed by dry etching the PZT layer. Subsequently, the Ti35 hard mask was dissolved with AZ 100 k remover at 70 °C, and the sample was cleaned in O_2 plasma. Finally, the sample was dehydrated and loaded in HF vapor phase etcher (Idonus VPE100) to expose the sample to an HF vapor at a substrate temperature of 40 °C. The SiO_2 etching process was monitored by looking through the microscope, and the process was carried on until the device looked fully suspended. Figure 4(a) shows an optical image of a fully suspended device. The length of the modulator region is 100 μm.

To verify that the device is fully suspended, a cross section of one of the devices on the chip was made using a focused ion beam

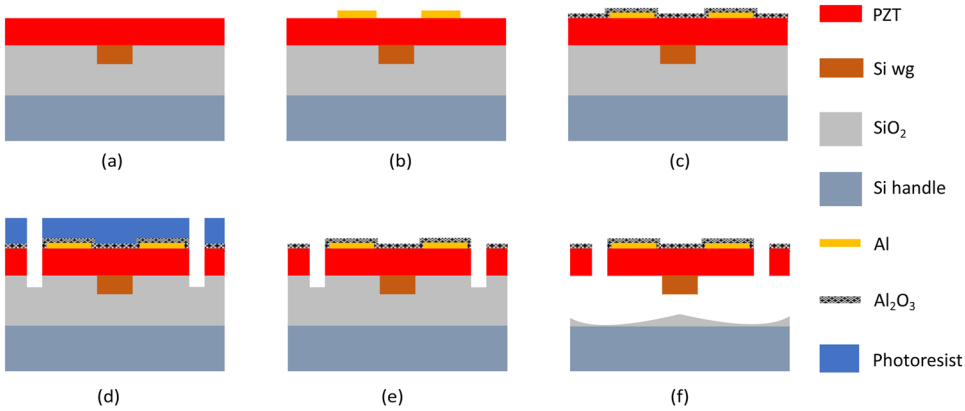

FIG. 3. Schematic diagram showing the process flow. (a) PZT deposition on planarized Si PIC, (b) fabrication of the Al electrodes, (c) ALD deposition of 50 nm Al_2O_3 and partial etching of Al_2O_3 film from the contact pads, (d) etching through Al_2O_3/PZT layers to create etch windows, (e) removal of the photoresist mask followed by dehydration of the sample, and (f) HF vapor exposure to etch SiO_2.

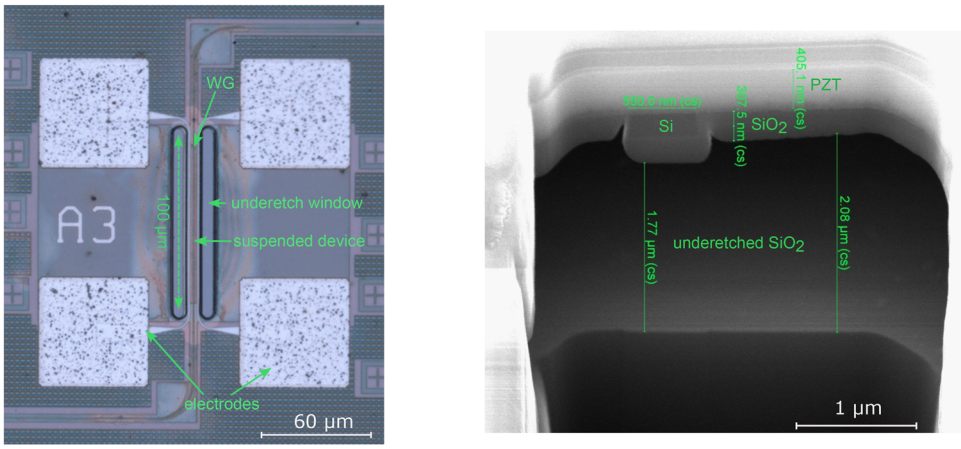

FIG. 4. (a) Optical image (top view) of a fabricated EOMT. (b) Cross-sectional SEM image of a suspended device.

(FIB). The scanning electron microscope (SEM) image of the cross section is shown in Fig. 4(b), which confirms the waveguide is fully underetched as ~2 μm of SiO_2 is removed. However, a ~280 nm thick layer of SiO_2 still seems to be present under the PZT and surrounding the Si waveguide. Even after another exposure to HF vapor for about 5 min, this residue remained.

IV. RESULTS AND DISCUSSION

A heterodyne setup was used to measure the optical phase modulation[28] from the EOMT. A continuous wave (CW) laser at 1590 nm with an output power of 14 dBm was used to couple the light into the chip through a grating coupler. When the phase of the light into the chip is modulated, the output optical spectrum shows sidebands around the reference acousto-optic modulator (AOM) driving frequency. The strength of the phase modulation was measured in terms of modulation efficiency given by $\eta^2 = 10 \times \log_{10}(P_{sideband}/P_{AOM})$. Here, $P_{sideband}$ is the peak power of the sideband, and P_{AOM} is the peak power of the AOM signal. For a detailed description of the measurement technique, see Ref. 28.

Figure 5(a) shows the modulation efficiency η^2 measured on the device EOMT1, driven with a 12 dBm RF driving signal (P_{RF}), before and after poling the PZT film. EOMT1 parameters are described in Table I. Before poling, the as-deposited PZT shows four main peaks labeled B_0, B_1, B_2, and B_3. These peaks possibly originate from shear mode actuation through the transverse electric field (in-plane) with respect to the PZT domains, which are oriented out-of-plane after deposition.[26–28] Moreover, the transverse electric field generates a weak EO effect. This is manifested through the

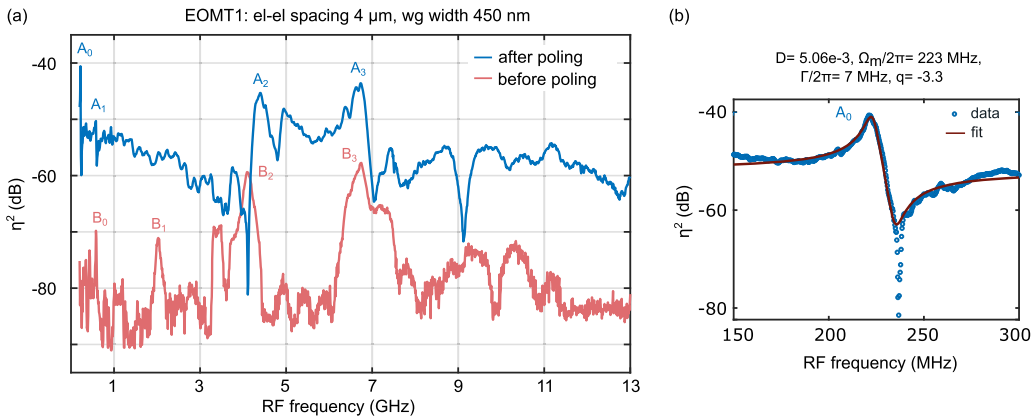

FIG. 5. (a) Modulation efficiency (η^2) of EOMT1 driven with 12 dBm RF power. (b) Measurement data of the primary Fano resonance and fit with the Fano formula. Note that the deviation between the data and the fit at lower values (i.e., below −65 dB) looks exaggerated due to the logarithmic scale. On a linear scale, this deviation would be negligible.

TABLE I. EOMT1 and EOMT2 parameters.

	el-el separation (μm)	Si waveguide width (nm)	P_{RF} (dBm)
EOMT1	4	450	12
EOMT2	4	550	14

low broadband (non-resonance) modulation response. The weak EO response furthermore explains the absence of any Fano response, as explained in Fig. 2. Next, the PZT film was poled to align its domain polarization along the applied in-plane electric field. For the poling process, a DC voltage (40 V) was applied to the electrodes at room temperature for about 40–60 min.

After the poling process, EOMT1 shows several Fano-like (asymmetric) resonances. The Fano resonance peaks are labeled A_0 (~220 MHz), A_1 (~570 MHz), A_2 (~4.4 GHz), and A_3 (~6.73 GHz). As explained above, these Fano resonances appear due to the interference between the broadband EO response and a narrowband mechanical mode excitation. Since the strongest Fano resonance was observed around 220 MHz, an additional measurement was carried out to collect more data points around this resonance (A_0). These measured data were then fitted with Eq. (5). Both the data and the fit are presented in Fig. 5(b). We can clearly see that the dip of the Fano curve goes to the noise floor, with an extinction ratio and slope of ~41 dB and 1.194 $\times 10^{-3}$ rad/MHz, respectively. The higher frequency Fano resonance (A_3) has an extinction ratio and slope of ~21 dB and 0.035 3 $\times 10^{-3}$ rad/MHz, respectively.

Figure 6 shows the electrical measurement on EOMT1 with a VNA. The Smith plot shown in Fig. 6(a) confirms the capacitive behavior of the device and electromechanical actuation at certain frequencies. The curve representing the magnitude of the reflection scattering parameter S_{11} presented in Fig. 6(b) shows five main transduction dips: V_0 (~229 MHz), V_1 (~600 MHz), V_2 (~2.50 GHz), V_3 (~3.31 GHz), and V_4 (~6.76 GHz). The dips V_0, V_1, V_3, and V_4 correspond to the resonance peaks A_0, A_1, A_2, and A_3 from EOMT1, as presented in Fig. 5(a).

Since $P_{sideband}/P_{AOM} = \alpha(L)^2/4$, as discussed in Refs. 28, $\alpha(L)$ can be extracted from the measured η^2 as $\alpha(L) = 2 \times 10^{(\eta^2/20)}$. From this, the voltage required for a π-phase shift can be calculated as $V_\pi = \pi\, V_p/\alpha(L)$, where V_p is the voltage applied to the device. In several works,[24,28,29] $V_\pi L$ is presented as a figure of merit for a resonance based modulator (e.g., an acousto-optic modulator). Often, while calculating the voltage V_p corresponding to an applied RF power, the load impedance (Z_L) is conveniently taken as 50 Ω, which may not be correct, as the actual Z_L depends on the device and its material properties. For example, the Z_L of a typical EO modulator is frequency-dependent due to its capacitive nature. Moreover, Z_L can sharply change at the mechanical resonance due to the electromechanical coupling. Hence, to estimate the actual Z_L of our device, a vector network analyzer (VNA) measurement was carried out. From this Z_L, the actual load voltage was calculated as $V_L = V_p = |Z_L/(Z_L + Z_S)| \times V_S$, where $Z_S = 50\ \Omega$ is the source impedance and V_S is the source voltage. For a detailed discussion of the electrical characterization, see Appendix A. Now, using the data from both electrical and optical measurements, the figure of merit for EOMT1 was calculated, as presented in Table II. The table illustrates that $V'_\pi L$ calculated taking into account the actual load impedance Z_L is higher than $V_\pi L$ calculated using 50 Ω as the load impedance. This is because our capacitive device has a higher impedance at lower frequencies.

Figure 7(a) shows the modulation efficiency η^2 measured for EOMT2, driven with 14 dBm P_{RF}. EOMT2 parameters are described in Table I. This measurement was taken after poling the PZT film. Here, we see several Lorentzian peaks, Fano peaks, and dips. We believe this might be due to a stronger perturbation in the wider Si waveguide. Figure 7(b) shows a detail around the primary mode (A_0) of EOMT2 and a fit to the Fano curve. We notice that the Fano curve has an opposite polarity compared to that of the similar mode from EOMT1.

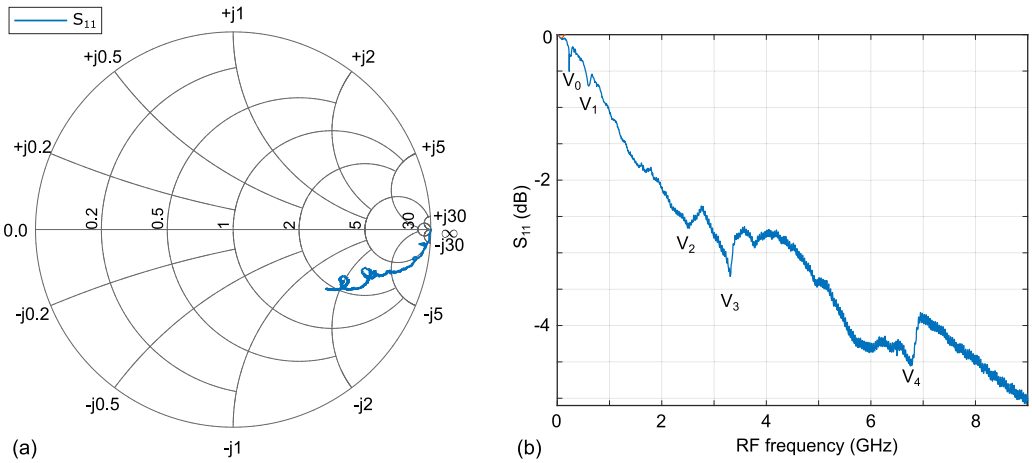

FIG. 6. Electrical measurement with VNA on EOMT1 (a) Smith plot showing the capacitive behavior of the device and (b) magnitude of S_{11} showing the transduction dips.

TABLE II. Figure of merit calculated from the measured modulation efficiency (η^2) and S_{11} of EOMT1.

Peak	$\Omega/2\pi$ (MHz)	η^2 (dB)	α (rad)	$V_\pi L$ (V cm) @ $Z_L = Z_o = 50\ \Omega$	$Z_L/50\ (\Omega)$	$V'_\pi L$ (V cm) @Z_L
A_0	220	−40.6	0.019	2.12	6.33-j23.07	4.19
A_1	570	−50.50	0.006	6.47	4.35-j10.22	12.46
A_2	4400	−45.30	0.011	3.64	2.49-j2.95	6.15
A_3	6730	−43.6	0.013	3.00	2.33-j1.86	4.67

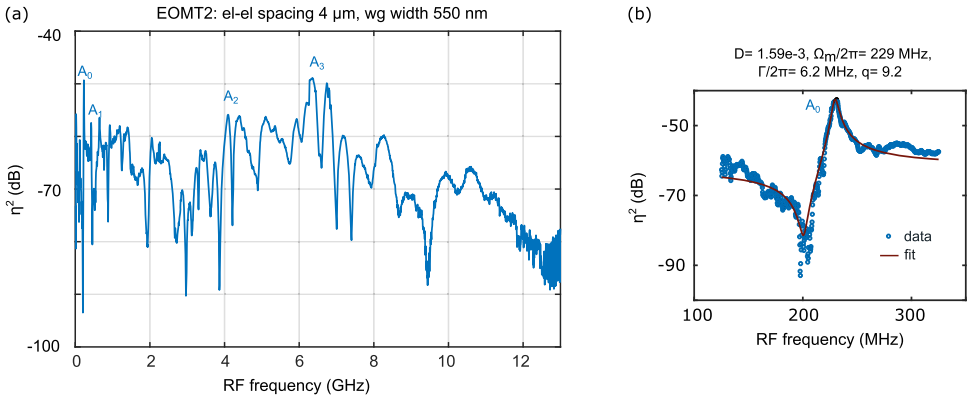

FIG. 7. (a) Modulation efficiency (η^2) for EOMT2 driven with 14 dBm RF power. (b) Measurement data of the primary Fano resonance and fit with the Fano formula. Again, here the deviation between the data and the fit looks exaggerated at the lower values due to the logarithmic scale.

To understand this polarity difference, we calculated the strain-optic overlap integral along the x-direction (Γ_{SOxx}) for the PZT and Si layers as described as follows:

$$\Gamma_{SOxx} = -\frac{n_{eff}^3}{2}\frac{\int_D E^*(\text{sign}(p_{ij}) * S_{xx})\ E\ dr}{\int_D E^* \varepsilon E\ dr}. \quad (6)$$

Here, p_{ij} is the photoelastic coefficient of the material. For the in-plane poled PZT, $p_{ij} = p_{33}$ and $\text{sign}(p_{33}) =$ "+ ." Whereas, for Si, $p_{ij} = p_{11}$ and $\text{sign}(p_{11}) =$ "− ".[30,31] The expression for Γ_{SOxx} is similar to Δn_{eff}^{PE} except for the value of p_{ij}. The p_{ij} values were omitted for both layers as the accurate value for PZT is not known. In Fig. 8,

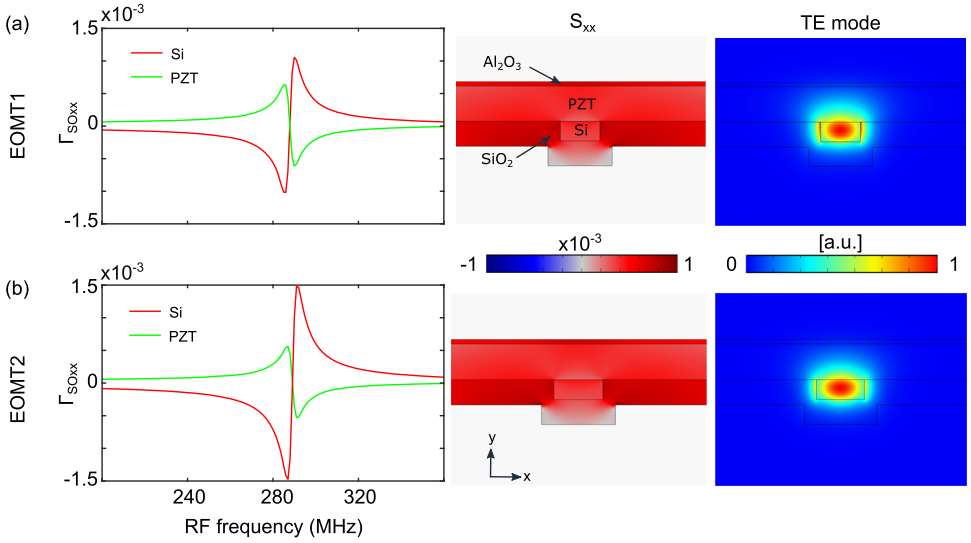

FIG. 8. Strain-optic overlap integral (Γ_{SOxx}), surface plot of the strain-x component (S_{xx}) at ~290 MHz, and TE mode profile from (a) EOMT1 and (b) EOMT2.

we see that the strain-optic overlap (Γ_{SOxx}) from the two layers is in opposite polarity due to the opposite signs of their p_{ij}. This indicates that the net polarity of the PE modulation depends on which layer is dominating. In addition, as expected, we observe that Γ_{SOxx} in Si increases when the waveguide width is increased. We believe this trade-off between the PE contribution from the Si and PZT layers could be the reason for the opposite polarity of EOMT2 compared to that of EOMT1.

V. CONCLUSION AND OUTLOOK

We presented piezoelectrically driven Fano resonances in a Si PIC by integrating a photonic-compatible PZT thin film and underetching the device. The resulting suspended structure, when subjected to microwave excitation at its resonance frequency, exhibits strong mechanical oscillations. The interference between the mechanical resonance-induced modulation and the broadband modulation from the electro-optic effect results in a Fano-like response in the modulation spectrum. At the primary mechanical mode, we obtained a very high modulation extinction of 41 dB. We also observed Fano resonances at frequencies up to 6.7 GHz, but with a lower extinction of 21 dB. Our results demonstrate an efficient generation of Fano resonances in PICs, opening up new possibilities for the development of highly sensitive and energy-efficient devices for a range of applications, including sensing, filtering, and modulation.

ACKNOWLEDGMENTS

This work was partially supported by the EU Commission through Grant Agreement No. 732894 (FET proactive HOT) and UGent Grant No. BOFGOA2020000103. Hannes Rijckaert and Gilles F. Feutmba acknowledge the support and funding from the Research Foundation-Flanders (FWO), under Grant Nos. 1273621N and 1S68218N, as a postdoctoral fellow and an SB-Ph.D. fellow, respectively. Thanks to Laurens Bogaert, Joris Van Kerrebrouck, Geert Morthier, and Xin Yin for the discussion on the transmission line.

AUTHOR DECLARATIONS

Conflict of Interest

The authors have no conflicts to disclose.

Author Contributions

I. Ansari: Conceptualization (lead); Data curation (lead); Formal analysis (lead); Funding acquisition (supporting); Investigation (lead); Methodology (lead); Project administration (equal); Resources (lead); Software (lead); Validation (lead); Visualization (lead); Writing – original draft (lead); Writing – review & editing (lead). **G. F. Feutmba**: Investigation (supporting); Methodology (supporting); Resources (supporting); Validation (supporting); Writing – review & editing (supporting). **J. P. George**: Methodology (supporting); Resources (supporting); Writing – review & editing (supporting). **H. Rijckaert**: Investigation (supporting); Resources (supporting); Visualization (supporting); Writing – original draft (supporting); Writing – review & editing (supporting). **J. Beeckman**: Funding acquisition (equal); Investigation (supporting); Methodology (supporting); Project administration (equal); Resources (supporting); Supervision (equal); Validation (equal); Writing – original draft (supporting); Writing – review & editing (equal). **D. Van Thourhout**: Conceptualization (supporting); Funding acquisition (equal); Investigation (equal); Methodology (supporting); Project administration (equal); Resources (equal); Supervision (equal); Validation (equal); Writing – original draft (supporting); Writing – review & editing (equal).

DATA AVAILABILITY

The data that support the findings of this study are available from the corresponding author upon reasonable request.

APPENDIX A: ELECTRICAL CHARACTERIZATION

For the electrical characterization of our devices, a VNA (Keysight's Fieldfox N9917A) was used. Before the measurement, the VNA was calibrated in the required frequency range using a standard calibration substrate containing short, open, load, and through (SOLT) contacts. This calibration ensures that the impedance of the RF probe, connector, or cable is not taken into account while measuring the reflection scattering parameter (S_{11}) of the device under test (DUT).[32] The measured reflection parameter (S_{11}) is given by

$$S_{11} = \frac{Z_L - Z_o}{Z_L + Z_o}, \tag{A1}$$

where Z_o is the characteristic impedance (50 Ω) of the VNA and Z_L is the load impedance of the DUT.

The voltage drop on the load (V_L) is obtained by solving the transmission line equation for the circuit diagram shown in Fig. 9(a). The diagram shows the RF signal transfer from the source to the load via a transmission line of length l. Since our device is much shorter (100 μm) than the shortest RF wavelength (~1.9 cm at 10 GHz), it can be regarded as a lumped element, i.e., no traveling wave within the device. Assuming our transmission line (coax cable connecting the RF source to the DUT) is lossless, the voltage at a given position (x) of the transmission line,[33]

$$V_x = V_o^+ e^{-j\beta x} + V_o^- e^{j\beta x}, \tag{A2}$$

where V_o^+ and V_o^- are the forward and backward voltage amplitudes, respectively, β is the RF wave propagation constant, and x is the position of the transmission line with respect to the reference. The voltage drop over the load (at $x = 0$),

$$V_L = V_o^+ + V_o^-. \tag{A3}$$

Here, the two unknown constants V_o^+ and V_o^- can be obtained from the boundary conditions. Since the reflection parameter (S_{11}) is the ratio of the reflected signal to the input signal, S_{11} at the end of the transmission line,

$$\begin{aligned} S_{11} &= \frac{V_o^-}{V_o^+} = \frac{Z_L - Z_o}{Z_L + Z_o}, \\ \Rightarrow\ V_o^- &= V_o^+ \left(\frac{Z_L - Z_o}{Z_L + Z_o}\right), \end{aligned} \tag{A4}$$

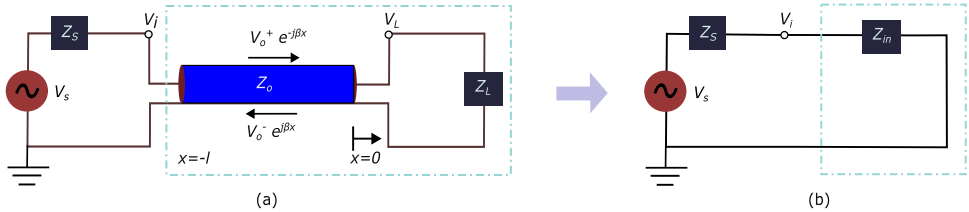

FIG. 9. (a) Circuit diagram showing the RF signal propagation through a transmission line of length *l* to the load and (b) an equivalent circuit diagram in terms of the input impedance (Z_{in}).

where Z_0 (=50 Ω) is the characteristic impedance of the transmission line. Now, for the second boundary condition, we look at the beginning of the transmission line. The impedance at the input of the transmission line is given as follows:[33]

$$Z_{in} = Z_o\left(\frac{Z_L + jZ_o \tan(\beta l)}{Z_o + jZ_L \tan(\beta l)}\right).$$

This Z_{in} allows simplification of the transmission line circuit, as shown in Fig. 9(b).

The voltage at the input of the transmission line,

$$V_i = \frac{Z_{in}}{Z_s + Z_{in}} V_s, \tag{A5}$$

where Z_s and V_s are the source impedance and source voltage, respectively.

However, from Eq. (A2), the voltage at the input transmission line ($x = -l$) can be formulated as follows:

$$V_i = V_o^+ e^{j\beta l} + V_o^- e^{-j\beta l}. \tag{A6}$$

Assuming the RF source impedance (Z_s) is equal to the transmission line characteristic impedance (Z_o = 50 Ω), the algebra on Eqs. (A4)–(A6) gives

$$V_o^+ = \frac{V_s}{2} e^{-j\beta l}. \tag{A7}$$

From (A3), (A4), and (A7), the load voltage,

$$\begin{aligned} V_L &= V_o^+ + V_o^+\left(\frac{Z_L - Z_o}{Z_L + Z_o}\right) \\ &= \frac{V_s}{2} e^{-j\beta l}\left(1 + \frac{Z_L - Z_o}{Z_L + Z_o}\right) \\ &= \frac{Z_L}{Z_L + Z_o} V_s\, e^{-j\beta l}. \end{aligned} \tag{A8}$$

Hence, the voltage amplitude at the load,

$$|V_L| = \left|\frac{Z_L}{Z_L + Z_o}\right| |V_s|. \tag{A9}$$

Note that when a certain power (P_{RF}) is set to the RF generator, it generates a source signal such that the set power dissipates over a load of impedance Z_o = 50 Ω,

$$\Rightarrow P_{RF} = \frac{V_{rms}^2}{Z_o} = \frac{V_{disp}^2}{2Z_o},$$

$$\Rightarrow V_{disp} = \sqrt{2P_{RF}Z_o},$$

where V_{rms} and V_{disp} are the root-mean-square and amplitude voltages shown on the RF generator display, respectively. Since the RF generator assumes a 50 Ω load (same as the source impedance), the actual voltage amplitude generated by the RF source,

$$|V_s| = 2V_{disp} = 2\sqrt{2P_{RF}Z_o}. \tag{A10}$$

From Eqs. (A9) and (A10),

$$|V_L| = \left|\frac{Z_L}{Z_L + Z_o}\right| \times 2V_{disp} = \left|\frac{Z_L}{Z_L + Z_o}\right| \times 2\sqrt{2P_{RF}Z_o}. \tag{A11}$$

Hence, for a given driving power, the actual load voltage on our device can be obtained using Eq. (A11). We can see that when $Z_L = Z_o$, the load voltage $V_L = V_{disp}$, as expected. However, when $Z_L \gg Z_o$, $V_L \to 2V_{disp} = V_s$.

APPENDIX B: SIMULATION OF THE PIEZOELECTRIC ACTUATION

We used COMSOL, a finite element method (FEM) based solver, to simulate the piezoelectric actuation of our EOMT. We defined the geometry of the cross section of the device as shown in Fig. 10. The thickness of the layers was set as t_{AlO} = 50 nm, t_{Al} = 100 nm, t_{PZT} = 400 nm, t_{Si} = 220 nm, and t_{SiO} = 280 nm. The width of the structures was set as w_{el} = 1 μm, w_{Si} = 450. The separation between the electrodes was set at 4 μm, and the total width of the device (w_{beam}) was taken at 6.5 μm. These geometrical values were estimated based on the optical microscope image and the SEM image, as shown in Fig. 4.

In the first step of the electromechanical simulation, an electrostatic solver was used to calculate the electric field from a voltage applied to the electrodes. The PZT domain polarization was then set along these electric field lines. This was done to account for the process whereby the PZT film was poled by a sufficiently high voltage applied to the electrodes. In the second step, an RF input signal (amplitude 1 V) was applied to the electrodes, and the piezoelectric actuation was simulated in the frequency domain. We opted for a generalized plane strain model for the solid mechanics interface to calculate the steady state solution in the frequency domain.[34] This

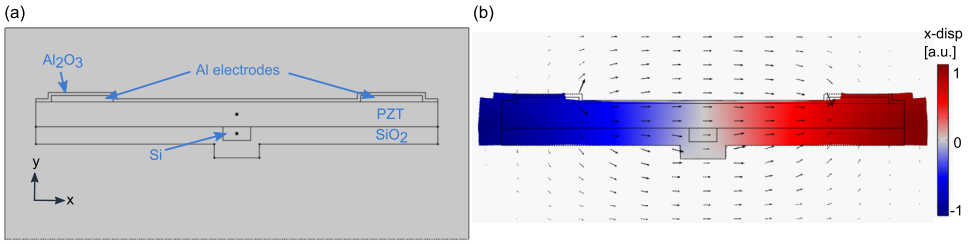

FIG. 10. (a) 2D simulation setup in the Comsol multiphysics and (b) surface plot showing the x-displacement at the resonance frequency of ~ 288 MHz; the arrows denote the applied electric field.

model assumes that the suspended structure is not strictly restrained in the out-of-simulation plane direction (which was the case in our EOMT due to the extra underetching), the strains are independent of the out-of-plane coordinate, and the length of the structure (out-of-simulation plane direction) is much larger than the cross section area (in-plane). Finally, a mode solver was used to simulate the TE mode profile of the EOMT at 1550 nm.

Figure 10(b) illustrates the simulated x-displacement of an EOMT at a mechanical resonance of 288 MHz. The arrows show the direction of the electric field from the voltage applied to the electrodes. The PZT material properties used in the electromechanical simulation were taken from the PZT-5A,[35] and the refractive index used in the optical simulation was $n_{PZT} = 2.4$.[17] For other materials, standard values were taken from the literature.

APPENDIX C: CALCULATION OF THE n_{eff} MODULATION

When a suspended structure is actuated with the piezoelectric effect, it can experience a change in the effective refractive index (Δn_{eff}) through the following mechanisms:

A. Moving boundary (MB) effect

When a mechanical motion is exerted on the waveguide, the waveguide boundaries are distorted. This changes the electric field distribution at the boundaries in accordance with Maxwell's continuity law. If the optical mode field lines experience sharp medium changes, the mechanical distortion can have a significant impact on n_{eff}. This change can be estimated by integrating the distortion and the optical field components at the interface, as described as follows:[36]

$$\Delta n_{eff}^{MB} = \frac{n_{eff}}{2} \frac{\oint_B (Q \cdot \hat{n}) \left(E_{\parallel}^* \Delta\varepsilon E_{\parallel} - D_{\perp}^* \Delta\varepsilon^{-1} D_{\perp} \right) dS}{\int_D E^* \varepsilon E \, dr}, \tag{C1}$$

where Q is the displacement field, $\hat{n}$ is the outward normal vector of the boundary, and E and D are the electric field and the displacement field of the optical mode, respectively. The subscripts $\parallel$ and $\perp$ denote parallel and perpendicular components at the boundary, respectively. ε is the permittivity of the waveguide mode. $\Delta\varepsilon = \varepsilon_1 - \varepsilon_2$ and $\Delta\varepsilon^{-1} = \varepsilon_1^{-1} - \varepsilon_2^{-1}$, where ε_1 and ε_2 are the permittivity of the medium 1 (denser medium) and medium 2, respectively. Here, D stands for the 2D cross section domain of the waveguide.

In Fig. 11(a), Δn_{eff}^{MB} calculated from the different interfaces of the EOMT1 are shown. For this calculation, only the interfaces closer to the mode profile were selected, as other interfaces had negligible effect. Here, we observe that the strongest contribution comes from the Si–PZT interface. This is because of the strong index contrast and the optical field density, as can be seen from the mode profile in Fig. 8(a). On the other hand, the outer-most SiO_2–air interface has a weaker MB effect as both the index contrast and the optical field are comparatively lower at this interface.

B. Photo-elastic (PE) effect

In addition to the distortion of the electric field density at the boundary, the mechanical perturbation also influences the bulk properties of the waveguide medium. This volumetric perturbation affects the electron density of the dielectric medium,[37] thus changing the n_{eff}. This index change can be calculated as follows:[31]

$$\Delta n_{eff}^{PE} = -\frac{n_{eff}^3}{2} \frac{\int_D E^* \boldsymbol{pS} \, E \, dr}{\int_D E^* \varepsilon E \, dr}, \tag{C2}$$

where E is the electric field of the waveguide mode, $\boldsymbol{p}$ is the photoelastic tensor of the waveguide medium, and $\boldsymbol{S}$ is the strain field. In the waveguide mode region, the PZT film was in-plane poled. So, the 2D simulation plane of the PZT material is a ZX plane. For such crystal, orientation of PZT (a tetragonal crystal with 3m point group symmetry), $\boldsymbol{pS}$ can be expanded as follows:

$$\boldsymbol{pS} = \begin{bmatrix} p_{33} & p_{31} & p_{31} & 0 & 0 & 0 \\ p_{13} & p_{11} & p_{12} & 0 & 0 & 0 \\ p_{13} & p_{12} & p_{11} & 0 & 0 & 0 \\ 0 & 0 & 0 & p_{66} & 0 & 0 \\ 0 & 0 & 0 & 0 & p_{44} & 0 \\ 0 & 0 & 0 & 0 & 0 & p_{44} \end{bmatrix} \begin{bmatrix} S_{xx} \\ S_{yy} \\ S_{zz} \\ S_{yz} \\ S_{zx} \\ S_{xy} \end{bmatrix}.$$

Therefore, for the PZT layer, Eq. (C2) can be approximated as follows: considering a TE mode ($E_x \gg E_y$),

$$\Delta n_{eff}^{PE} = -\frac{n_{eff}^3}{2} \frac{\int_D E_x^* (p_{33} S_{xx} + p_{31} S_{yy} + p_{31} S_{zz}) \, E_x \, dr}{\int_D E^* \varepsilon E \, dr}. \tag{C3}$$

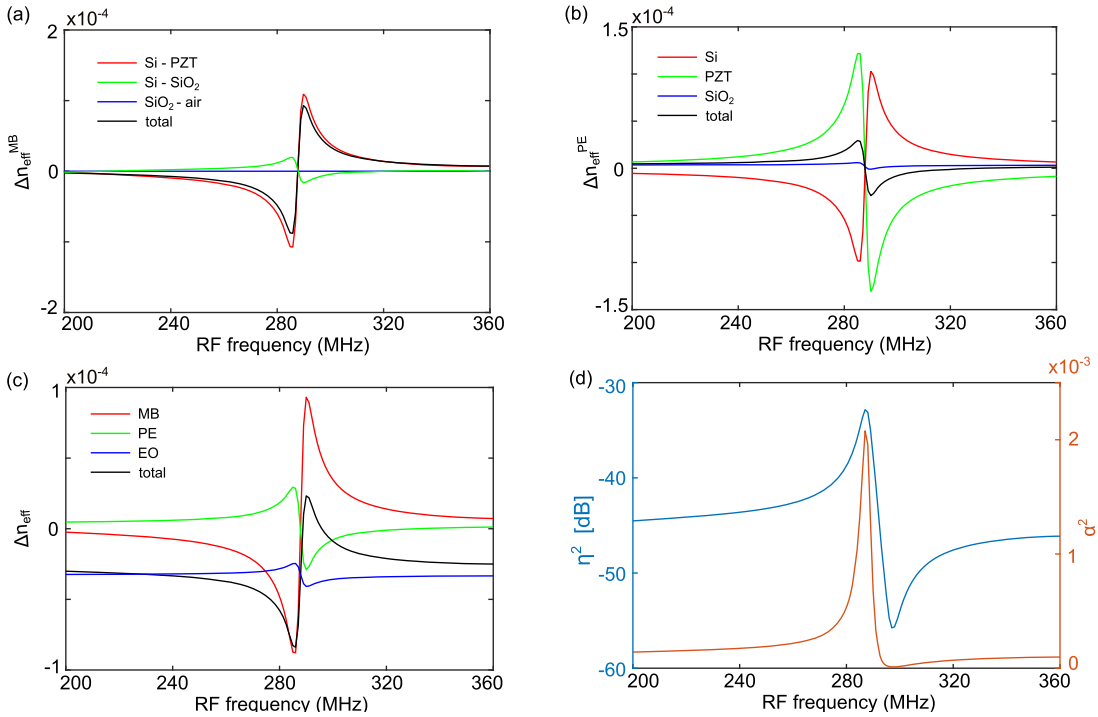

FIG. 11. Calculation of the index modulation from the simulated results: (a) Δn_{eff}^{MB} plot for different interfaces in the waveguide mode region, (b) Δn_{eff}^{PE} plot for different layers in the waveguide system, (c) Δn_{eff} contribution from different mechanisms, and (d) log and linear plot of the net phase modulation.

Thus, we require two unknown material parameters, p_{33} and p_{31}, to calculate the PE contribution Δn_{eff}^{PE} from the PZT layer. It should be noted that the PZT thin film is a relatively new material for photonic applications because it is traditionally grown using a Pt buffer layer (optically lossy). That is why the photoelastic coefficients $(\boldsymbol{p})$ of such thin films have not been properly estimated. In Ref. 38, it was demonstrated that for ABO_3 type ferroelectric thin films, $p_{33} > p_{31}$, and[30] p_{33} can be roughly assumed to be around 0.60. Using these values as starting parameters, the experimental result shown in Fig. 5(b) was fitted with the simulation result to find the unknown parameters for the PZT film. From the least squares fitting, we obtained $p_{33} \approx 0.48$ and $p_{31} \approx 0.40$. In addition, we also extracted the other unknown PZT parameter, Pockels' coefficient $r_{33}^{eff} \approx 75$ pm/V, to calculate the EO modulation. Note that these values may not be accurate. Since the material parameters used in the simulation may be different from those in our PZT film, nevertheless, these values can be used to get a qualitative understanding of Fano's behavior.

For the Si crystal orientation [110], a rotational transformation was applied to the photoelastic tensor of Si taken,[31] resulting in the following coefficients: $p_{11} = -0.090$, $p_{12} = 0.013$, $p_{21} = p_{12}$, and $p_{22} = p_{11}$. For SiO_2, $p_{11} = 0.121$, $p_{12} = 0.270$ were taken from.[39] Now, using these coefficients and the simulation results, Δn_{eff}^{PE} was calculated for each layer as shown in Fig. 11(b). Here, we observe that Δn_{eff}^{PE} from Si has opposite polarity compared to the rest of the layers. This is because the strongest photoelastic coefficient for Si, p_{11}, has a negative sign.

C. Electro-optic (EO) effect

When an electric field is applied to a dielectric medium, its polarization change leads to a change in n_{eff}. If the dielectric medium is a non-centrosymmetric crystal (i.e., PZT), Δn_{eff} is linearly proportional to the applied electric field. This proportionality constant is the Pockels' coefficient (r_{ij}). If the applied electric field or optical power is very high, the second-order electro-optic effect, also known as the Kerr effect, can also contribute to the index change. For the co-planar waveguide and electrodes in our EOMT, the main driving field is along the x-direction $(\mathscr{E}_x)$. If the effective Pockels' coefficient along the x-direction is assumed to be r_{33}^{eff}, the effective index change can be estimated as follows:[40]

$$\Delta n_{eff}^{EO} = -\frac{\varepsilon_0\, n_{eff}^5}{2} \frac{\int_D \left[E_x^* (r_{33}^{eff} \mathscr{E}_x) E_x\right] dr}{\int_D E^* \varepsilon E\, dr}. \tag{C4}$$

Figure 11(c) shows the contribution to Δn_{eff} from each mechanism described above. Here, we can see that Δn_{eff}^{EO} has a rather weak frequency dependence compared to the frequency response from other mechanisms. This validates our assumption of the

frequency-independent EO response for deriving the Fano expression as described in Eq. (4). Therefore, the total change in n_{eff} in the suspended device is

$$\Delta n_{eff}^{total} = \Delta n_{eff}^{MB} + \Delta n_{eff}^{PE} + \Delta n_{eff}^{EO}. \quad \text{(C5)}$$

Figure 11(d) shows the modulation efficiency (η^2) and the phase modulation amplitude (α^2) calculated from Δn_{eff}^{total}. Here, L and λ were taken as 100 μm and 1590 nm, respectively. Thus, we see a Fano resonance when the EOMT1 is piezoelectrically driven with an RF signal. This simulation result corresponds to the measured Fano response reported in Fig. 5(b). The deviation in the simulation result can be attributed to the difference in the parameters used in the simulation and the experiment.

REFERENCES

[1] U. Fano, "Effects of configuration interaction on intensities and phase shifts," Phys. Rev. **124**, 1866 (1961).
[2] A. Li and W. Bogaerts, "An actively controlled silicon ring resonator with a fully tunable Fano resonance," APL Photonics **2**, 096101 (2017).
[3] G. Wang, T. Dai, J. Jiang, H. Yu, Y. Hao, Y. Wang, Y. Li, X. Jiang, and J. Yang, "Slope tunable Fano resonances in asymmetric embedded microring resonators," J. Opt. **19**, 025803 (2017).
[4] G. Zhao, T. Zhao, H. Xiao, Z. Liu, G. Liu, J. Yang, Z. Ren, J. Bai, and Y. Tian, "Tunable Fano resonances based on microring resonator with feedback coupled waveguide," Opt. Express **24**, 20187–20195 (2016).
[5] W. Zhang, W. Li, and J. Yao, "Optically tunable Fano resonance in a grating-based Fabry–Perot cavity-coupled microring resonator on a silicon chip," Opt. Lett. **41**, 2474–2477 (2016).
[6] K. Y. Yang, J. Skarda, M. Cotrufo, A. Dutt, G. H. Ahn, M. Sawaby, D. Vercruysse, A. Arbabian, S. Fan, A. Alù, and J. Vučković, "Inverse-designed non-reciprocal pulse router for chip-based lidar," Nat. Photonics **14**, 369–374 (2020).
[7] Q. Xu, P. Dong, and M. Lipson, "Breaking the delay-bandwidth limit in a photonic structure," Nat. Phys. **3**, 406–410 (2007).
[8] Y. Yu, M. Heuck, H. Hu, W. Xue, C. Peucheret, Y. Chen, L. K. Oxenløwe, K. Yvind, and J. Mørk, "Fano resonance control in a photonic crystal structure and its application to ultrafast switching," Appl. Phys. Lett. **105**, 061117 (2014).
[9] J. Zhang, X. L. Roux, E. Ruran-Valdeiglesias, C. Alonso-Ramos, D. Marris-Morini, L. Vivien, S. He, and E. Cassan, "Generating Fano resonances in a single-waveguide nanobeam cavity for efficient electro-optical modulation," ACS Photonics **5**, 4229–4237 (2018).
[10] D. Bekele, Y. Yu, K. Yvind, and J. Mork, "In-plane photonic crystal devices using Fano resonances," Laser Photonics Rev. **13**, 1900054 (2019).
[11] R. Ortuño, M. Cortijo, and A. Martínez, "Fano resonances and electromagnetically induced transparency in silicon waveguides loaded with plasmonic nanoresonators," J. Opt. **19**, 025003 (2017).
[12] T. Huang, S. Zeng, X. Zhao, Z. Cheng, and P. P. Shum, "Fano resonance enhanced surface plasmon resonance sensors operating in near-infrared," Photonics **5**, 23 (2018).
[13] M. F. Limonov, "Fano resonance for applications," Adv. Opt. Photonics **13**, 703–771 (2021).
[14] J.-H. Wu, J.-Y. Gao, J.-H. Xu, L. Silvestri, M. Artoni, G. C. La Rocca, and F. Bassani, "Ultrafast all optical switching via tunable Fano interference," Phys. Rev. Lett. **95**, 057401 (2005).
[15] D. Marpaung, J. Yao, and J. Capmany, "Integrated microwave photonics," Nat. Photonics **13**, 80–90 (2019).
[16] J. Zhang, X. Leroux, E. Durán-Valdeiglesias, C. Alonso-Ramos, D. Marris-Morini, L. Vivien, S. He, and E. Cassan, "Generating Fano resonances in a single-waveguide silicon nanobeam cavity for efficient electro-optical modulation," ACS photonics **5**, 4229–4237 (2018).
[17] K. Alexander, J. P. George, J. Verbist, K. Neyts, B. Kuyken, D. Van Thourhout, and J. Beeckman, "Nanophotonic Pockels modulators on a silicon nitride platform," Nat. Commun. **9**, 3444 (2018).
[18] I. Ansari, D. V. Thourhout, J. P. George, G. F. Feutmba, and J. Beeckman, "Acousto-optic modulation in a Si-waveguide," in *2021 IEEE 17th International Conference on Group IV Photonics (GFP)* (IEEE, 2021), pp. 1–2.
[19] J. P. George, P. F. Smet, J. Botterman, V. Bliznuk, W. Woestenborghs, D. Van Thourhout, K. Neyts, and J. Beeckman, "Lanthanide-assisted deposition of strongly electro-optic PZT thin films on silicon: Toward integrated active nanophotonic devices," ACS Appl. Mater. Interfaces **7**, 13350–13359 (2015).
[20] E. Kamenetskii, A. Sadreev, and A. Miroshnichenko, "Fano resonances in optics and microwaves," in *Springer Series in Optical Sciences Book Series*, 219 (Springer, 2018) (in press).
[21] R. Soref and B. Bennett, "Electrooptical effects in silicon," IEEE J. Quantum Electron. **23**, 123–129 (1987).
[22] P. T. Rakich, C. Reinke, R. Camacho, P. Davids, and Z. Wang, "Giant enhancement of stimulated Brillouin scattering in the subwavelength limit," Phys. Rev. X **2**, 011008 (2012).
[23] R. Van Laer, B. Kuyken, D. Van Thourhout, and R. Baets, "Interaction between light and highly confined hypersound in a silicon photonic nanowire," Nat. Photonics **9**, 199–203 (2015).
[24] E. A. Kittlaus, W. M. Jones, P. T. Rakich, N. T. Otterstrom, R. E. Muller, and M. Rais-Zadeh, "Electrically driven acousto-optics and broadband non-reciprocity in silicon photonics," Nat. Photonics **15**, 43–52 (2021).
[25] P. P. Absil, P. De Heyn, H. Chen, P. Verheyen, G. Lepage, M. Pantouvaki, J. De Coster, A. Khanna, Y. Drissi, D. Van Thourhout, and J. Van Campenhout, "Imec iSiPP25G silicon photonics: A robust CMOS-based photonics technology platform," SPIE Proc. **9367**, 166–171 (2015).
[26] J. P. George, P. F. Smet, J. Botterman, V. Bliznuk, W. Woestenborghs, D. Van Thourhout, K. Neyts, and J. Beeckman, "Lanthanide-assisted deposition of strongly electro-optic PZT thin films on silicon: Toward integrated active nanophotonic devices," ACS Appl. Mater. Interfaces **7**, 13350–13359 (2015).
[27] I. Ansari, G. F. Feutmba, E. Dieussaert, J. P. George, J. Beeckman, and D. V. Thourhout, "PZT based actuator for an efficient electro-optomechanical interaction in Si-photonic integrated circuits," SPIE Proc. **12004**, 266–269 (2022).
[28] I. Ansari, J. P. George, G. F. Feutmba, T. Van de Veire, A. Pandey, J. Beeckman, and D. Van Thourhout, "Light modulation in silicon photonics by PZT actuated acoustic waves," ACS Photonics **9**, 1944–1953 (2022).
[29] C. Huang, H. Shi, L. Yu, K. Wang, M. Cheng, Q. Huang, W. Jiao, and J. Sun, "Acousto-optic modulation in silicon waveguides based on piezoelectric aluminum scandium nitride film," Adv. Opt. Mater. **10**, 2102334 (2022).
[30] K. Takeda, T. Hoshina, H. Takeda, and T. Tsurumi, "Electro-optic effect and photoelastic effect of feroelectric relaxors," Jpn J. Appl. Phys. **55**, 10TB05 (2016).
[31] D. Biegelsen, "Frequency dependence of the photoelastic coefficients of silicon," Phys. Rev. B **12**, 2427 (1975).
[32] A. M. E. Safwat and L. Hayden, "Sensitivity analysis of calibration standards for SOLT and LRRM," in *58th ARFTG Conference Digest* (IEEE, 2001), Vol. 40, pp. 1–10.
[33] M. Steer, *Microwave and RF Design* (NC State University, 2019).
[34] COMSOL, How to Model Generalized Plane Strain with COMSOL Multiphysics (URL Accessed 15 July 2023).
[35] Z. Butt, R. A. Pasha, F. Qayyum, Z. Anjum, N. Ahmad, and H. Elahi, "Generation of electrical energy using lead zirconate titanate (PZT-5A) piezoelectric material: Analytical, numerical and experimental verifications," J. Mech. Sci. Technol. **30**, 3553–3558 (2016).
[36] K. C. Balram, M. Davanço, J. Y. Lim, J. D. Song, and K. Srinivasan, "Moving boundary and photoelastic coupling in GaAs optomechanical resonators," Optica **1**, 414–420 (2014).
[37] H. Mueller, "Theory of the photoelastic effect of cubic crystals," Phys. Rev. **47**, 947 (1935).
[38] R. Nayak, V. Gupta, and K. Sreenivas, "Studies on acousto-optical interaction in epitaxial thin film heterostructures," J. Phys. D: Appl. Phys. **32**, 380 (1999).
[39] R. Dixon, "Photoelastic properties of selected materials and their relevance for applications to acoustic light modulators and scanners," J. Appl. Phys. **38**, 5149–5153 (1967).
[40] R. W. Boyd, *Nonlinear Optics* (Academic Press, 2020).